



MOX-Report No. 13/2017

**Optimized Schwarz Methods for circular flat interfaces  
and geometric heterogeneous coupled problems**

Gigante, G.; Vergara, C.

MOX, Dipartimento di Matematica  
Politecnico di Milano, Via Bonardi 9 - 20133 Milano (Italy)

[mox-dmat@polimi.it](mailto:mox-dmat@polimi.it)

<http://mox.polimi.it>

# Optimized Schwarz Methods for circular flat interfaces and geometric heterogeneous coupled problems

Giacomo Gigante<sup>1</sup>, Christian Vergara<sup>2</sup>

February 28, 2017

<sup>1</sup> Dipartimento di Ingegneria gestionale, dell'informazione e della produzione,  
Università degli Studi di Bergamo, Italy, [giacomo.gigante@unibg.it](mailto:giacomo.gigante@unibg.it)

<sup>2</sup> MOX, Dipartimento di Matematica, Politecnico di Milano, Italy,  
[christian.vergara@polimi.it](mailto:christian.vergara@polimi.it)

**Keywords:** Optimized Schwarz Method; cylindrical domains; geometric multi-scale; Bessel functions

## Abstract

In this work, we focus on the Optimized Schwarz Method for circular flat interfaces and geometric heterogeneous coupling. In the first case, we provide a convergence analysis for the diffusion-reaction problem and jumping coefficients and we apply the general optimization procedure developed in *Gigante and Vergara, Numer. Math., 131(2), 369–404, 2015*. In the numerical simulations, we discuss how to choose the range of frequencies in the optimization and the influence of the Finite Element and projection errors on the convergence. In the second case, we consider the coupling between a three-dimensional and a one-dimensional diffusion-reaction problem and we develop a new optimization procedure. The numerical results highlight the suitability of the theoretical findings.

## 1 Introduction

The Optimized Schwarz Method (OSM) is a well established Domain Decomposition method based on looking for efficient parameters in Robin-like interface conditions [30, 25]. This method has been considered for many problems, such as the advection-reaction-diffusion problem [16, 26], the Helmholtz equation [17, 31], the shallow-water equations [35], the Maxwell's equations [5], the fluid-structure interaction problem [20, 43, 22, 23], and the scattering problem [38].

From a geometric perspective, this method has been used for flat unbounded interfaces [16, 26, 17, 31, 35, 5, 38], circular interfaces [18, 19], cylindrical interfaces [21, 43, 22, 23], and spherical interfaces [22]. In this paper, we address for

the three-dimensional (3D) case a flat interface that, unlike previous works on this topic, is not an unbounded surface. Rather, we consider here the case of a flat circular interface. Analogously, for the overlapping case, the interface region is given here by a cylinder instead of a 3D strip.

The study of circular flat interfaces is of particular interest when a Partial Differential Equation (PDE) is solved in a cylindrical domain which is split in two (or more) cylinders with interfaces orthogonal to the axial direction. For example, this is the case when parallel computing is performed to speed up the numerical solution of the problem at hand, or for jumping material parameters. Here, we provide a convergence analysis of the partitioned procedure arising in this context for a diffusion-reaction problem, and we discuss some optimal choices of the interface parameters. We also show some numerical results that highlight the effectiveness of our theoretical findings, and highlight the relationship between the convergence and the Finite Element errors.

In the second part of the paper, we address the split of a cylinder into two non-overlapping cylinders, where one of them (let say the distal one) is substituted by a geometric reduced one-dimensional model, where only the axial coordinate survives. This leads to a *geometric multiscale* model, where the geometric heterogeneous coupling between 3D and 1D models is addressed. This coupled problem has been studied in a general framework in [29, 2], and widely considered in hemodynamic applications, see e.g. [7, 4, 33, 37]. The interface conditions appearing in partitioned algorithms for the 3D-1D coupled problem in hemodynamics involve Dirichlet and Neumann data [9], the total pressure [10, 3], or the characteristic variables [7]. Other type of partitioned algorithms were obtained in [4] by considering a Lagrange multipliers mortaring, and in [29, 32, 3] by introducing the interface equation. Here, we address the case of Robin-type interface conditions for the reaction-diffusion problem. In particular, we study the convergence of the resulting Schwarz method and we propose optimal values for the interface parameters. Finally, we show some numerical results highlighting the effectiveness of our theoretical findings.

The outline of this paper is as follows. In Section 2 we address the case of the generalized Schwarz algorithm obtained in the 3D-3D splitting, whereas in Section 3 the one arising from the 3D-1D coupling. For each of these two sections, we provide a convergence analysis of the related generalized Schwarz algorithm, we discuss possible optimization procedures to find effective values of the interface parameters, and we show the numerical results.

## 2 The 3D-3D splitting case

### 2.1 Problem setting

Referring to Figure 1, we consider the following coupled problem in the overlapping subdomains  $\Omega_1 = \{(r, \varphi, z) : 0 \leq r < R, 0 \leq \varphi < 2\pi, -\infty < z < H\}$  and

$$\Omega_2 = \{(r, \varphi, z) : 0 \leq r < R, 0 \leq \varphi < 2\pi, 0 < z < +\infty\}$$

$$-\mu_1 \Delta u_1 + \gamma_1 u_1 = 0 \quad \mathbf{x} \in \Omega_1, \quad (1a)$$

$$u_1|_{\Sigma} = u_1|_{z \rightarrow -\infty} = 0, \quad (1b)$$

$$u_1 = u_2 \quad \mathbf{x} \in \Gamma_1, \quad (1c)$$

$$\mu_1 \frac{\partial u_1}{\partial z} = \mu_2 \frac{\partial u_2}{\partial z} \quad \mathbf{x} \in \Gamma_2, \quad (1d)$$

$$-\mu_2 \Delta u_2 + \gamma_2 u_2 = 0 \quad \mathbf{x} \in \Omega_2, \quad (1e)$$

$$u_2|_{\Sigma} = u_2|_{z \rightarrow \infty} = 0, \quad (1f)$$

where  $\mu_1, \mu_2, \gamma_1, \gamma_2$  are given positive parameters,  $\Sigma$  is the lateral surface, and we considered the homogeneous case in view of the convergence analysis. The interfaces  $\Gamma_1$  and  $\Gamma_2$  are located at  $z = H \geq 0$  and  $z = 0$ , respectively.

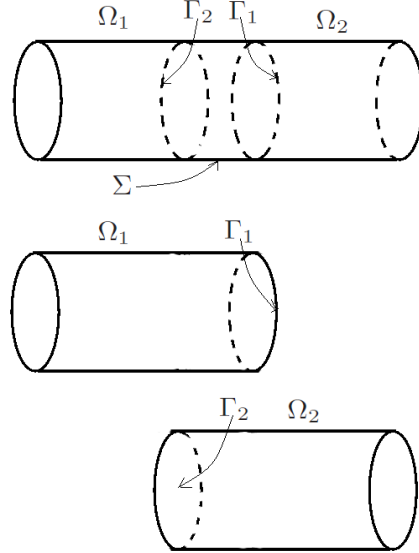


Figure 1: Unsplit computational domain (up) and overlapping subdomains (bottom).

Introducing two linear operators  $\mathcal{S}_1 \neq \mathcal{S}_2$  and  $\omega \in (0, 1]$ , we consider the following *generalized Schwarz* method for the solution of the previous problem, obtained by linearly combining the interface equations (1c)-(1d):

Given  $\tilde{u}_2^{(0)}$ , at each iteration  $n > 0$ , until convergence

1. solve the problem in  $\Omega_1$ :

$$-\mu_1 \Delta u_1^{(n)} + \gamma_1 u_1^{(n)} = 0 \quad \mathbf{x} \in \Omega_1, \quad (2a)$$

$$u_1^{(n)}|_{\Sigma} = u_1^{(n)}|_{z \rightarrow -\infty} = 0, \quad (2b)$$

$$\mathcal{S}_1 u_1^{(n)} + \mu_1 \frac{\partial u_1^{(n)}}{\partial z} = \mathcal{S}_1 \tilde{u}_2^{(n-1)} + \mu_2 \frac{\partial \tilde{u}_2^{(n-1)}}{\partial z} \quad \mathbf{x} \in \Gamma_1; \quad (2c)$$

2. solve the problem in  $\Omega_2$ :

$$-\mu_2 \Delta u_2^{(n)} + \gamma_2 u_2^{(n)} = 0 \quad \mathbf{x} \in \Omega_2, \quad (3a)$$

$$u_2^{(n)}|_{\Sigma} = u_2^{(n)}|_{z \rightarrow \infty} = 0, \quad (3b)$$

$$\mathcal{S}_2 u_2^{(n)} + \mu_2 \frac{\partial u_2^{(n)}}{\partial z} = \mathcal{S}_2 u_1^{(n)} + \mu_1 \frac{\partial u_1^{(n)}}{\partial z} \quad \mathbf{x} \in \Gamma_2; \quad (3c)$$

3. relaxation step:  $\tilde{u}_2^{(n)} = \omega u_2^{(n)} + (1 - \omega) \tilde{u}_2^{(n-1)}$ .

## 2.2 Convergence analysis

We report in what follows a convergence result of the previous partitioned algorithm. In this first analysis, we assume that  $u_1$  and  $u_2$  do not depend on the angular coordinate  $\varphi$ , i.e.  $u_j = u_j(r, z)$ ,  $j = 1, 2$ . Although simplified, the following analysis will highlight important features of the coupling with a flat circular interface.

Let  $R$  be the radius of the cylinder and  $\{x_k\}_{k=1}^{+\infty}$  the positive zeros of the Bessel function  $J_0$ . Unlike the case of a flat unbounded interface, here we do not consider the Fourier transform of our unknowns, rather, their Fourier-Bessel expansions in the variable  $r \in [0, R]$  [27]:

$$u_j(r, z) = \sum_{k=1}^{+\infty} \hat{u}_j(k, z) J_0\left(x_k \frac{r}{R}\right), \quad (4)$$

where

$$\hat{u}_j(k, z) = \frac{2}{R^2 J_1(x_k)^2} \int_0^R u_j(r, z) J_0\left(x_k \frac{r}{R}\right) r dr.$$

Notice that such functions satisfy the condition  $u_j|_{\Sigma} = 0$ .

We have the following result.

**Proposition 1** *The reduction factor related to the iterations (2)-(3), in the case  $\omega = 1$  and  $u_1 = u_1(r, z)$ ,  $u_2 = u_2(r, z)$ , is given by*

$$\rho_{3D-3D}(k) = \frac{\sigma_2 + \mu_1 \beta_{1,k}}{\sigma_2 - \mu_2 \beta_{2,k}} \cdot \frac{\sigma_1 - \mu_2 \beta_{2,k}}{\sigma_1 + \mu_1 \beta_{1,k}} e^{-(\beta_{1,k} + \beta_{2,k})H}, \quad (5)$$

where  $\sigma_j = \sigma_j(k)$ ,  $j = 1, 2$ , are the symbols of  $\mathcal{S}_j$  related to the Fourier-Bessel expansion, and

$$\beta_{j,k} = \sqrt{\frac{\gamma_j}{\mu_j} + \frac{x_k^2}{R^2}}. \quad (6)$$

**Proof.** Since the expression of the Laplacian in cylindrical coordinates is

$$\Delta w = \frac{1}{r} \frac{\partial}{\partial r} \left( r \frac{\partial w}{\partial r} \right) + \frac{1}{r^2} \frac{\partial^2 w}{\partial \varphi^2} + \frac{\partial^2 w}{\partial z^2},$$

and since the eigenfunctions of

$$\frac{1}{r} \frac{\partial}{\partial r} \left( r \frac{\partial w}{\partial r} \right)$$

are the functions  $J_0(\alpha r)$  with eigenvalues  $-\alpha^2$ ,  $\alpha \in \mathbb{R}$ , we have for each  $j = 1, 2$

$$\begin{aligned} \Delta u_j &= \frac{1}{r} \frac{\partial}{\partial r} \left( r \frac{\partial u_j}{\partial r} \right) + \frac{\partial^2 u_j}{\partial z^2} \\ &= \sum_{k=1}^{+\infty} \hat{u}_j(k, z) \frac{1}{r} \frac{\partial}{\partial r} \left( r \frac{\partial \left( J_0 \left( x_k \frac{r}{R} \right) \right)}{\partial r} \right) + \sum_{k=1}^{+\infty} \frac{\partial^2 \hat{u}_j(k, z)}{\partial z^2} J_0 \left( x_k \frac{r}{R} \right) \\ &= \sum_{k=1}^{+\infty} \left( -\frac{x_k^2}{R^2} \right) \hat{u}_j(k, z) J_0 \left( x_k \frac{r}{R} \right) + \sum_{k=1}^{+\infty} \frac{\partial^2 \hat{u}_j(k, z)}{\partial z^2} J_0 \left( x_k \frac{r}{R} \right). \end{aligned}$$

The equations  $\gamma_j u_j - \mu_j \Delta u_j = 0$  therefore become

$$\begin{aligned} \gamma_j \sum_{k=1}^{+\infty} \hat{u}_j(k, z) J_0 \left( x_k \frac{r}{R} \right) - \mu_j \sum_{k=1}^{+\infty} \left( -\frac{x_k^2}{R^2} \right) \hat{u}_j(k, z) J_0 \left( x_k \frac{r}{R} \right) - \mu_j \sum_{k=1}^{+\infty} \frac{\partial^2 \hat{u}_j(k, z)}{\partial z^2} J_0 \left( x_k \frac{r}{R} \right) &= 0 \\ \sum_{k=1}^{+\infty} \left( \left( \frac{\gamma_j}{\mu_j} + \frac{x_k^2}{R^2} \right) \hat{u}_j(k, z) - \frac{\partial^2 \hat{u}_j(k, z)}{\partial z^2} \right) J_0 \left( x_k \frac{r}{R} \right) &= 0. \end{aligned}$$

This gives

$$\left( \frac{\gamma_j}{\mu_j} + \frac{x_k^2}{R^2} \right) \hat{u}_j(k, z) - \frac{\partial^2 \hat{u}_j(k, z)}{\partial z^2} = 0$$

for every  $k = 1, 2, 3, \dots$ . The condition  $u_1|_{z=-\infty} = 0$  and  $u_2|_{z=\infty} = 0$  give

$$\hat{u}_1(k, z) = C_1(k) e^{\beta_{1,k} z} \quad \hat{u}_2(k, z) = C_2(k) e^{-\beta_{2,k} z}, \quad (7)$$

where  $\beta_{j,k}$  are given by (6) and  $C_j(k)$ ,  $j = 1, 2$ , are two functions determined as usual by the interface conditions.

Now, by writing the Fourier-Bessel expansions of the interface conditions (2c) and (3c) and using (7), we obtain

$$\begin{aligned} (\sigma_1 + \mu_1 \beta_{1,k}) C_1^{(n)}(k) e^{\beta_{1,k} H} &= (\sigma_1 - \mu_2 \beta_{2,k}) C_2^{(n-1)}(k) e^{-\beta_{2,k} H}, \\ (\sigma_2 - \mu_2 \beta_{2,k}) C_2^{(n)}(k) &= (\sigma_2 + \mu_1 \beta_{1,k}) C_1^{(n)}(k). \end{aligned}$$

Taking as usual for the reduction factor to quantity  $C_2^{(n)}(k)/C_2^{(n-1)}(k)$  (see e.g. [16]), we obtain the thesis.  $\square$

We consider now the case without overlap,  $H = 0$ . In this case, we can use the general convergence analysis provided in [22]. In particular, we have the following result.

**Proposition 2** *In the case without overlap ( $H = 0$ ), iterations (2)-(3), with  $\omega = 1$  and  $u_1 = u_1(r, z)$ ,  $u_2 = u_2(r, z)$ , converge if and only if*

$$\begin{aligned} \sigma_2 < \sigma_1 \text{ and } \left( \sigma_1 + \frac{\mu_1\beta_{1,k} - \mu_2\beta_{2,k}}{2} \right) \left( \sigma_2 + \frac{\mu_1\beta_{1,k} - \mu_2\beta_{2,k}}{2} \right) &< \left( \frac{\mu_1\beta_{1,k} + \mu_2\beta_{2,k}}{2} \right)^2, \quad \text{or} \\ \sigma_2 > \sigma_1 \text{ and } \left( \sigma_1 + \frac{\mu_1\beta_{1,k} - \mu_2\beta_{2,k}}{2} \right) \left( \sigma_2 + \frac{\mu_1\beta_{1,k} - \mu_2\beta_{2,k}}{2} \right) &> \left( \frac{\mu_1\beta_{1,k} + \mu_2\beta_{2,k}}{2} \right)^2. \end{aligned}$$

**Proof.** Referring to Theorem 1 in [22], we observe that the hypothesis for its application are satisfied since  $\mu_2\beta_{2,k} > -\mu_1\beta_{1,k}$  for all  $k$ , see [22]. Thus, the thesis follows by a straightforward application of this theorem.  $\square$

### 2.3 Optimization procedures

We refer again to [22], where a general way to provide optimal values of the interface parameters is provided for the case without overlap. We report, for the sake of exposition, only the case  $\mu_1 = \mu_2 = 1$ . We have the following result.

**Proposition 3** *There exist three numbers  $\rho_0 < 1$ ,  $p_-$ ,  $p_+$ , such that the reduction factor (5) for  $H = 0$  satisfies*

$$\rho_{3D-3D}(k) \leq \rho_0, \quad \forall k = k_{min}, \dots, k_{max},$$

$$\text{provided that } \sigma_1 = p, \sigma_2 = 2M - p, \text{ with } p \in [p_-, p_+] \text{ and } M = \frac{1}{2} \left( \sqrt{\gamma_2 + \frac{x_{k_{min}}^2}{R^2}} - \sqrt{\gamma_1 + \frac{x_{k_{min}}^2}{R^2}} \right).$$

*In particular, for the case  $\gamma_1 = \gamma_2 = \gamma$ , we have  $M = 0$ ,*

$$p_- = \frac{1 - \sqrt{\rho_0}}{1 + \sqrt{\rho_0}} \beta_{k_{max}} \quad p_+ = \frac{1 + \sqrt{\rho_0}}{1 - \sqrt{\rho_0}} \beta_{k_{min}}. \quad (8)$$

and

$$\rho_0 = \left( \frac{1 - \sqrt[4]{\frac{R^2\gamma + x_{k_{min}}^2}{R^2\gamma + x_{k_{max}}^2}}}{1 + \sqrt[4]{\frac{R^2\gamma + x_{k_{min}}^2}{R^2\gamma + x_{k_{max}}^2}}} \right)^2.$$

**Proof.** The thesis follows by the application of Theorem 2 in [22].  $\square$

The previous result gives us a range of constant values for the interface parameters which guarantees that the reduction factor is less than  $\rho_0 < 1$ , i.e. convergence independent of  $k$ .

## 2.4 Numerical results

### 2.4.1 Generalities

The numerical results presented here have been obtained by means of the Finite Element (FE) code *FreeFem++* ([www.freefem.org](http://www.freefem.org)).

In all the numerical experiments, we consider the cylinder  $\Omega = \{(r, \varphi, z) : 0 \leq r < R, 0 \leq \varphi < 2\pi, 0 < z < 2L\}$  split into two non-overlapping domains  $\Omega_1 = \{(r, \varphi, z) : 0 \leq r < R, 0 \leq \varphi < 2\pi, 0 < z < L\}$  and  $\Omega_2 = \{(r, \varphi, z) : 0 \leq r < R, 0 \leq \varphi < 2\pi, L < z < 2L\}$ , separated by the interface  $\Gamma = \{(r, \varphi, z) : 0 \leq r < R, 0 \leq \varphi < 2\pi, z = L\}$ . In our case, we have used  $R = 0.5$  and  $L = 2.5$ . Moreover, if not otherwise specified, we set  $\gamma_1 = \gamma_2 = 10$  and  $\mu_1 = \mu_2 = 1$ . As a consequence, we have  $M = 0$  in the estimates of Proposition 3.

The numerical solutions have been obtained by solving two-dimensional axi-symmetric problems. The corresponding meshes were formed by triangles, and the discretization parameter is  $h = R/10 = 0.05$ . The stopping criterion is given by

$$\int_{\Gamma} |u_1^{(n)} - u_1^{(n-1)}|^2 d\gamma \leq \varepsilon^2,$$

where  $\varepsilon = 10^{-7}$ . If not otherwise specified, we use P2 Finite Elements and we consider no relaxation, i.e.  $\omega = 1$ .

### 2.4.2 On the choice of the frequencies in the optimization procedure

In the above Proposition 3, the optimal interface parameters are established after an *a priori* evaluation of the relevant “frequency” parameters  $k$ . It is well known that when applying this method in a numerical simulation, certain frequencies can be considered irrelevant to the problem. For example, in the (two dimensional) classical approach to the problem, the interface is modeled as an unbounded line, and the continuous Fourier transform  $\int_{-\infty}^{+\infty} f(x)e^{-ixm} dx$  is used. When adapting this analysis to a particular case, only the frequencies  $m$  between two values  $M_{\min}$  and  $M_{\max}$  are considered. Indeed, one can disregard all frequencies smaller than  $M_{\min} = \pi/D$ , where  $D$  is a characteristic dimension of the effective interface used in the numerical experiment, as well as all frequencies greater than the Nyquist-Shannon frequency  $M_{\max} = \pi/h$ . The Fourier-Bessel expansion that we use here already takes into account the shape and dimensions of the interface. Thus, unlike the case of analysis for an unbounded interface, there is no reason to disregard any of the lower values of the “frequency” parameter  $k$ . On the other hand, in our two-dimensional axi-symmetric numerical simulations the interface reduces to the interval  $[0, R]$  and the mesh size is given by  $h = R/N$  for an integer  $N$ , with nodes, say,  $0 = r_1 < r_2 < \dots < r_N < r_{N+1} = R$ . In this situation one can disregard all the

values of  $k$  greater than  $N$ . Indeed, if  $k > N$  then the linear system

$$\begin{cases} u_2^{(0)}(r_1, L) = \alpha_1 J_0\left(\frac{x_1 r_1}{R}\right) + \dots + \alpha_k J_0\left(\frac{x_k r_1}{R}\right) \\ \dots \\ u_2^{(0)}(r_N, L) = \alpha_1 J_0\left(\frac{x_1 r_N}{R}\right) + \dots + \alpha_k J_0\left(\frac{x_k r_N}{R}\right) \end{cases}$$

has more variables than equations, and therefore will never have one solution only (we have not considered the equation corresponding to  $r_{N+1} = R$  since all the functions  $J_0(x_k r/R)$  vanish there). For this reason, when computing the optimal interface values in (2.8), all the values of  $k$  greater than  $R/h = N$  can be considered irrelevant to the problem.

In conclusion, according to the previous analysis, the shape and dimension of the interface and the size of the mesh allow us to disregard all frequency parameters  $k$  outside the interval  $[K_{min}, K_{max}]$ , where  $K_{min} = 1$  and  $K_{max} = R/h$ .

It is perhaps worth observing here that the value  $K_{max} = R/h = N$  corresponds to the Nyquist-Shannon frequency  $\pi/h$  in the following sense: the function  $J_0\left(\frac{x_k r}{R}\right)$  with the highest possible value of  $k$ , that is  $J_0\left(\frac{x_N r}{R}\right)$ , performs exactly  $N$  half oscillations in the interval  $[0, R]$ , which means on average half oscillation for each interval of length  $h$ . Similarly, the functions  $e^{imx}$  with the highest possible value of  $m$ , that is  $e^{\pm i\pi x/h}$  perform exactly half oscillation for each interval of length  $h$ .

Thus, by the above observations, it is reasonable to choose an initial guess

$$u_2^{(0)}(r, L) = \sum_{k=k_1}^{k_2} \widehat{u_2^{(0)}}(k) J_0\left(x_k \frac{r}{R}\right),$$

with  $1 \leq k_1 \leq k_2 \leq K_{max}$ . From a theoretical point of view, no other frequencies appear in the iterative process other than those between  $k_1$  and  $k_2$ . For this reason the best possible choice in Proposition 3 should be  $k_{min} = k_1$  and  $k_{max} = k_2$ .

In the practical situation, however, as the iterations proceed, frequencies other than those strictly between  $k_1$  and  $k_2$  seem to appear, due to the Finite Element approximation. These new frequencies are not irrelevant to the computations, and it may therefore be better to choose different values of  $k_{min}$  and  $k_{max}$  than  $k_1$  and  $k_2$  respectively when applying Proposition 3.

In order to be able to detect the above described phenomenon in the practical situations, it is convenient to define the following *effective reduction factor*

$$\rho_h^{(n)} = \frac{\left(\int_{\Gamma} |u_1^{(n)} - u_1^{(n-1)}|^2 d\gamma\right)^{1/2}}{\left(\int_{\Gamma} |u_1^{(n-1)} - u_1^{(n-2)}|^2 d\gamma\right)^{1/2}}, \quad (9)$$

which is computable by the numerical experiments (it is in fact the ratio between two consecutive stopping criterium quantities). Notice that by the orthogonality of the functions  $J_0\left(\frac{x_k r}{R}\right)$ ,

$$\rho_h^{(n)} = \left( \sum_{k=1}^{+\infty} (\rho_{3D-3D}(k))^2 w_k \right)^{1/2}, \quad (10)$$

where

$$w_k = \frac{\left| \widehat{u_1^{(n-1)}}(k) - \widehat{u_1^{(n-2)}}(k) \right|^2 \pi R^2 J_1^2(x_k)}{\int_{\Gamma} |u_1^{(n-1)} - u_1^{(n-2)}|^2 d\gamma}. \quad (11)$$

Thus, the effective reduction factor  $\rho_h^{(n)}$  can be considered as a weighted  $\ell^2(\mathbb{N}, \{w_k\}_{k=1}^{+\infty})$  average of the reduction factor  $\{\rho_{3D-3D}(k)\}_{k=1}^{+\infty}$ . For a generic initial guess  $u_2^{(0)}$ , one can *a posteriori* deduce that the leading frequency in the increment  $\left(\int_{\Gamma} |u_1^{(n-1)} - u_1^{(n-2)}|^2 d\gamma\right)^{1/2}$  is one of the values of  $k$  for which  $\rho_h^{(n)} \approx \rho_{3D-3D}(k)$ . Indeed, if  $\rho_h^{(n)} \approx \rho_{3D-3D}(\bar{k})$  for some  $\bar{k}$ , then one can extrapolate that in (10), all the weights are negligible except for  $w_{\bar{k}}$ , and this means precisely that the  $\bar{k}$ -th Fourier-Bessel coefficient of  $u_1^{(n-1)} - u_1^{(n-2)}$  is sensibly bigger than the others.

In the forthcoming results, we will analyze the convergence history for different choices of  $k_1$ ,  $k_2$ ,  $k_{min}$  and  $k_{max}$ , all included in the range  $[K_{min}, K_{max}] = [1, R/h]$ . In order to make the exposition clearer, we recall that  $K_{min}$  and  $K_{max}$  are the extreme frequencies compatible with the mesh,  $k_1$  and  $k_2$  the extreme frequencies appearing in the initial guess, whereas  $k_{min}$  and  $k_{max}$  the extreme frequencies used in the application of (8) for the optimization.

### 2.4.3 $k_1 = k_2 = 1$

In the first set of numerical simulations, we consider in the initial guess only the first value of  $k$ , namely  $k = 1$ . Thus, in principle we should have  $u_2^{(0)} = J_0\left(\frac{x_1 r}{R}\right)$ . We want to investigate first the production of sources of error generated only by the FE error. Thus, we approximate  $J_0\left(\frac{x_1 r}{R}\right)$  with a parabola, in order to have a vanishing projection error onto the FE space. In particular, we set

$$u_2^{(0)} = 1 - \left(\frac{r}{R}\right)^2.$$

Observe that the corresponding Fourier-Bessel coefficients  $\widehat{u_2^{(0)}}(k)$  from (11) are small for  $k \neq 1$ , but not vanishing. In particular, they decrease in modulus as  $k$  increases.

As a first choice, we set  $k_{min} = k_{max} = 1$  in the optimization procedure, i.e. we exploit the fact that the main contribution in the initial guess is given by  $k = 1$ , thus ignoring the presence of other frequencies. Owing to the estimates (8),

we obtain  $p_- = p_+ = 5.75$ . The numerical simulation converges in 8 iterations. In Table 1 we report the reduction factors as a function of  $k$  estimated a priori by means of (5) and the effective reduction factors as a function of the number of the iteration  $n$  estimated by means of (9). We report only some values in correspondence of the most significant  $k$  and  $n$ .

A priori reduction factors (5)	Effective reduction factors (9)
$\rho_{3D-3D}(1) = 0.0$	$\rho_h^{(3)} = 0.005$
$\rho_{3D-3D}(2) = 0.110$	$\rho_h^{(4)} = 0.124$
$\rho_{3D-3D}(3) = 0.257$	$\rho_h^{(5)} = 0.166$
$\rho_{3D-3D}(4) = 0.372$	$\rho_h^{(6)} = 0.216$
$\rho_{3D-3D}(5) = 0.460$	$\rho_h^{(7)} = 0.249$
$\rho_{3D-3D}(10) = 0.686$	$\rho_h^{(8)} = 0.271$

Table 1: Left: estimated reduction factors for selected values of  $k$ . Right: effective reduction factors for selected values of the iteration  $n$ . Case  $k_1 = k_2 = 1$  and  $k_{min} = k_{max} = 1$ .

From these results we observe that the a priori reduction factor in correspondence of  $k = 1$  is as expected vanishing, and increasing values of  $\rho_{3D-3D}$  are obtained for increasing  $k$ . Notice that that the effective reduction factor in Table 1, right column, reaches a value which is very similar to  $\rho_{3D-3D}(3) = 0.257$ . This means that the leading value is  $k = 3$ . This is the result of the balance between small (large) values of the Fourier-Bessel coefficient for  $k$  large (small) and large (small) values of the corresponding  $\rho_{3D-3D}$ . In particular, although characterized by large values of the reduction factor (see Table 1, left column) the high frequencies seem to not influence the convergence. Probably, also the FE error plays a role in determining the leading value of  $k$ , dumping and/or emphasizing some frequencies. This point is under investigation.

As a second choice, we set  $k_{min} = K_{min} = 1$  and  $k_{max} = K_{max} = R/h = 10$  in the optimization procedure, i.e. we ignore that the main contribution in the initial guess comes from  $k = 1$  and we consider all the frequencies appearing in the initial guess. In this case, the estimates (8) lead to  $p_- = p_+ = 18.79$ . The numerical simulation converges in 11 iterations. In Table 2 we report again some significant values of the reduction factors as a function of  $k$  estimated a priori by means of (5) and of the effective reduction factors as a function of the number of the iteration  $n$  estimated by means of (9).

From these results, first we observe that the a priori reduction factor given by the optimal choice (8) is not vanishing for  $k = 1$ . Instead, it features its maximum values for  $k = 1$  and  $k = 10$ , that is the extreme values of the range of possible  $k$ 's. This is in accordance with the optimality procedure of Proposition 3 which is based on finding a range of constant (i.e. independent of  $k$ ) values for the interface parameters that leads to a small reduction factor independently of

A priori reduction factors (5)	Effective reduction factors (9)
$\rho_{3D-3D}(1) = 0.282$	$\rho_h^{(3)} = 0.282$
$\rho_{3D-3D}(2) = 0.058$	$\rho_h^{(4)} = 0.282$
$\rho_{3D-3D}(3) = 0.001$	$\rho_h^{(5)} = 0.283$
$\rho_{3D-3D}(4) = 0.014$	$\rho_h^{(6)} = 0.283$
$\rho_{3D-3D}(5) = 0.053$	$\rho_h^{(7)} = 0.283$
$\rho_{3D-3D}(6) = 0.101$	$\rho_h^{(8)} = 0.283$
$\rho_{3D-3D}(7) = 0.150$	$\rho_h^{(9)} = 0.283$
$\rho_{3D-3D}(8) = 0.197$	$\rho_h^{(10)} = 0.283$
$\rho_{3D-3D}(9) = 0.241$	$\rho_h^{(11)} = 0.283$
$\rho_{3D-3D}(10) = 0.282$	

Table 2: Left: estimated reduction factors for selected values of  $k$ . Right: effective reduction factors for selected values of the iteration  $n$ . Case  $k_1 = k_2 = 1$  and  $k_{min} = 1, k_{max} = 10$ .

$k$ . Second, we highlight that this maximum value (0.282) is in fact coincident with the effective reduction factor. This means that  $k = 1$  is the leading value of  $k$  in the practice computation (we exclude  $k = 10$  since in the previous numerical computations we deduced that the higher frequencies, although characterized by large reduction factors, do not provide important contributions to the error). In this case, although an error due to  $k = 2$  and  $k = 3$  is still present (as in the previous case), it is rapidly dumped by the corresponding small reduction factor ( $\rho_{3D-3D}(2) = 0.058, \rho_{3D-3D}(3) = 0.001$ ).

We repeated the same tests with initial guess

$$u_2^{(0)} = \frac{\sqrt{2}}{RJ_1(x_1)} J_0\left(\frac{x_1 r}{R}\right).$$

In the case  $k_{min} = k_{max} = 1$  one should obtain convergence in one iteration, because  $k = 1$  is the only frequency in the initial guess, and  $\rho_{3D-3D} = 0.0$ . In practice one obtains convergence in 7 iterations, with an effective reduction factor converging to  $\rho_h^{(7)} = 0.300$  and a leading frequency between  $k = 3$  and  $k = 4$ . This means that the projection onto the FE space introduces new frequencies that are not present in the initial guess. The results of the test with  $k_{min} = 1$  and  $k_{max} = 10$  are very similar to those obtained in the case of the parabola, with a clear leading frequency  $k = 1$ .

#### 2.4.4 $k_1 = k_2 = 10$

In the second set of numerical simulations, we consider in the initial guess only the value  $k = 10$ . Thus, we set

$$u_2^{(0)} = \frac{\sqrt{2}}{RJ_1(x_{10})} J_0\left(\frac{x_{10}r}{R}\right).$$

As a first choice, we set  $k_{min} = k_{max} = 10$  in the optimization procedure. Owing to the estimates (8), we obtain  $p_- = p_+ = 61.35$ . The numerical simulation converges in 22 iterations. In Table 3 we report the reduction factors as a function of  $k$  estimated a priori by means of (5) and the effective reduction factors as a function of the number of the iteration  $n$  estimated by means of (9). We report only some values in correspondance of the most significant  $k$  and  $n$ .

A priori reduction factors (5)	Effective reduction factors (9)
$\rho_{3D-3D}(1) = 0.686$	$\rho_h^{(3)} = 0.078$
$\rho_{3D-3D}(2) = 0.469$	$\rho_h^{(4)} = 0.351$
$\rho_{3D-3D}(3) = 0.307$	$\rho_h^{(5)} = 0.416$
$\rho_{3D-3D}(5) = 0.118$	$\rho_h^{(8)} = 0.658$
$\rho_{3D-3D}(6) = 0.066$	$\rho_h^{(10)} = 0.682$
$\rho_{3D-3D}(8) = 0.013$	$\rho_h^{(15)} = 0.687$
$\rho_{3D-3D}(9) = 0.003$	$\rho_h^{(20)} = 0.687$
$\rho_{3D-3D}(10) = 0.0$	$\rho_h^{(22)} = 0.687$

Table 3: Left: estimated reduction factors for selected values of  $k$ . Right: effective reduction factors for selected values of the iteration  $n$ . Case  $k_1 = k_2 = 10$  and  $k_{min} = k_{max} = 10$ .

As expected, in this case the a priori reduction factor is vanishing for  $k = 10$  and assumes increasing values for  $k$  decreasing. Again, we should expect convergence in one iteration. However, the presence of error sources due to the low values of  $k$  slows down the convergence, which is even slower than the previous case since the a priori reduction factors are higher. In particular, the effective reduction factor reaches a value that is in fact equal to  $\rho_{3D-3D}(1) = 0.686$ . Thus, the leading value is  $k = 1$ .

As a second choice, we set  $k_{min} = 1$  and  $k_{max} = R/h = 10$  in the optimization procedure, i.e. we ignore that only  $k = 10$  appears in the initial guess and we consider all the values of  $k$  predicted by the Shannon theorem. Of course, the estimates (8) lead again to  $p_- = p_+ = 18.79$ . The numerical simulation converges in 11 iterations. The values of the a priori reduction factor coincide by construction with those reported in Table 2, left column. The values of the effective reduction factors are in principle different, but in practice they coincide for  $n \geq 4$  with those reported in Table 2, right column.

Again, the leading value is  $k = 1$ , but the convergence is faster with respect to the previous case ( $k_{min} = k_{max} = 10$ ) since  $\rho_{3D-3D}(1)$  is smaller. This is a consequence of having included all the values of  $k$  in the optimization procedure, thus helping to dump the errors due to the small values of  $k$  introduced by the FE error.

As a third choice, we set  $k_{min} = 1$  and  $k_{max} = (R/h)/2 = 5$  in the optimization procedure, i.e. we consider only the smallest values of  $k$  among those allowed by the Shannon theorem. The estimates (8) lead to  $p_- = p_+ = 13.14$ . The numerical simulation converges in 9 iterations. In Table 4 we report the reduction factors as a function of  $k$  estimated a priori by means of (5) and the effective reduction factors as a function of the number of the iteration  $n$  estimates by means of (9). We report only some values in correspondance of the most significant  $k$  and  $n$ .

A priori reduction factors (5)	Effective reduction factors (9)
$\rho_{3D-3D}(1) = 0.153$	$\rho_h^{(3)} = 0.198$
$\rho_{3D-3D}(2) = 0.004$	$\rho_h^{(4)} = 0.203$
$\rho_{3D-3D}(3) = 0.021$	$\rho_h^{(5)} = 0.169$
$\rho_{3D-3D}(5) = 0.153$	$\rho_h^{(6)} = 0.160$
$\rho_{3D-3D}(7) = 0.279$	$\rho_h^{(7)} = 0.159$
$\rho_{3D-3D}(8) = 0.331$	$\rho_h^{(8)} = 0.160$
$\rho_{3D-3D}(10) = 0.419$	$\rho_h^{(9)} = 0.161$

Table 4: Left: estimated reduction factors for selected values of  $k$ . Right: effective reduction factors for selected values of the iteration  $n$ . Case  $k_1 = k_2 = 10$  and  $k_{min} = 1, k_{max} = 5$ .

Interestingly, in this case the number of iterations is the lowest one among the three choices of  $k_{min}$  and  $k_{max}$  and the effective reduction factor tends to a value which is in fact very similar to  $\rho_{3D-3D}(1)$  (notice that in this case by construction  $\rho_{3D-3D}(1) = \rho_{3D-3D}(5)$  and the optimization procedure produces higher values of the a priori reduction factor for  $k \geq 6$ ). The reason of this improvement should be ascribed to the projection error of the initial guess onto the FE space (P2 in this case). Indeed, if  $u_2^{(0)}$  was well projected, the error corresponding to  $k = 10$  (the only frequency present in the initial guess) should slow down the convergence with an effective reduction factor close to  $\rho_{3D-3D}(10) = 0.419$ . The same arguments hold true for the numerical errors corresponding to  $6 \leq k \leq 9$ , since the corresponding a priori reduction factors are greater than  $\rho_{3D-3D}(1)$ . This is probably due to the projection onto the FE space that dumps the contribution of the highest values of  $k$ , even of those characterizing the initial guess. To confirm these observations, we run the same test as above with P3 FE. In this case, we need 12 iterations to reach convergence for

the case  $k_{min} = 1$ ,  $k_{max} = 10$ , with an effective reduction factor approaching the value 0.294, and 13 iterations for the case  $k_{min} = 1$ ,  $k_{max} = 5$ , with an effective reduction factor approaching the value 0.329. Thus, the reduction of  $k_{max}$  does not produce an improvement in the convergence, suggesting that in this case the smaller projection error does not dump the high values of  $k$ . In the latter case, the effective reduction factor reaches a value (0.329) similar to  $\rho_{3D-3D}(8)$ , see Table 4, left column. Again, the contribution of the initial value  $k = 10$  is dumped, but in this case the contribution corresponding to  $k = 8$  is not.

#### 2.4.5 $k_1 = 1$ , $k_2 = 10$

In the third set of numerical simulations, we consider all the values of  $k$  compatible with the mesh in the initial guess, i.e. we set

$$u_2^{(0)} = \sum_{j=1}^{10} \frac{\sqrt{2}}{R J_1(x_j)} J_0\left(\frac{x_j r}{R}\right). \quad (12)$$

As a first choice, we set  $k_{min} = 1$ ,  $k_{max} = 10$  in the optimization procedure, i.e.  $p_- = p_+ = 18.79$ . The numerical simulation converges in 13 iterations. The effective reduction factor approaches the value 0.283 which is again very similar to  $\rho_{3D-3D}(1)$  (see Table 2, left column). As a second choice, we set  $k_{min} = 1$ ,  $k_{max} = 5$  in the optimization procedure, i.e.  $p_- = p_+ = 13.14$ . Again, the number of iterations to reach convergence decreases (10) and the effective reduction factor approaches a value (0.165) very similar to  $\rho_{3D-3D}(1)$  (see Table 4, left column).

These results confirm that the projection error dumps the contribution of the highest values of  $k$ . Accordingly, one could think to improve the convergence by considering only  $k = 1$  in the optimization procedure, i.e. by setting  $p_- = p_+ = 5.75$  (see Section 2.4.1). By doing so, the number of iterations to reach convergence is 16, with an effective reduction factor reaching the value 0.37, very similar to  $\rho_{3D-3D}(4)$  (see Table 1, left column). This means that we cannot reduce too much  $k_{max}$  since low values of  $k > 1$  give an important contribution to the error as a consequence of the FE error.

Once again, we run the same test with P3 FE. In this case, we need 13 iterations to reach convergence for the case  $k_{min} = 1$ ,  $k_{max} = 10$ , with an effective reduction factor approaching the value 0.284, and 13 iterations for the case  $k_{min} = 1$ ,  $k_{max} = 5$ , with an effective reduction factor approaching the value 0.321, similar to  $\rho_{3D-3D}(8)$ , see Table 4, left column. Again, the contribution of the initial value  $k = 10$  is dumped, but the contribution corresponding to  $k = 8$  is not. Thus, also in this case, for P3 FE the reduction of  $k_{max}$  does not produce an improvement of the convergence.

### 2.4.6 The case of discontinuous coefficients

We address here the case  $\gamma_1 = 100$ ,  $\gamma_2 = 1$  and we consider as initial guess the function reported in (12), that is a function presenting the whole range of frequencies from  $K_{min} = 1$  to  $K_{max} = R/h = 10$ . Referring to the quantities defined in Sect. 2.3, in Table 5 we report the results of the numerical experiments (for the definition of  $p_-$  and  $p_+$  in the case  $\gamma_1 \neq \gamma_2$  we refer to [22]).

FE	$k_{min}$	$k_{max}$	$M$	$\rho_0$	$p_-$	$p_+$	# iter	$\rho_h^{(n_0)}$
P2	1	10	-3.09	0.22	19.08	19.13	$n_0 = 11$	0.22
P2	1	5	-3.09	0.10	12.46	12.57	$n_0 = 9$	0.22
P3	1	10	-3.09	0.22	19.08	19.13	$n_0 = 11$	0.22
P3	1	5	-3.09	0.10	12.46	12.57	$n_0 = 12$	0.26

Table 5: Values of  $M$ ,  $\rho_0$  and of the optimal range of  $p$  provided by the estimates reported in Proposition 3. Case  $\gamma_1 = 100$ ,  $\gamma_2 = 1$ .

From these results, we observe that the range of optimal  $p$  predicted by Proposition 3 is very thin, thus in fact providing directly the optimal value of  $p$  also in the case of discontinuous coefficients. The same type of phenomenon described in the case of continuous coefficients can be observed here too. The projection of the initial guess onto the Finite Element space P2 cancels the higher frequencies, and this gives a better performance when one takes  $k_{max} = 5$ . On the other hand, when the P3 Finite Elements are used, the higher frequencies remain relevant to the problem and things behave as expected.

## 3 The 3D-1D splitting case

As observed in the Introduction, in some applications there is the need to couple a 3D problem with the corresponding reduced 1D model. In particular, referring to Figure 2 and to the notation of Section 2 and setting  $\Omega_{3D} = \Omega_1$ , we consider the following coupled problem:

$$-\Delta u_{3D} + \gamma u_{3D} = 0 \quad \mathbf{x} \in \Omega_{3D}, \quad (13a)$$

$$u_{3D}|_{\Sigma} = u_{3D}|_{z \rightarrow -\infty} = 0, \quad (13b)$$

$$\frac{1}{|\Gamma|} \int_{\Gamma} u_{3D} d\gamma = u_{1D}|_{z=0}, \quad (13c)$$

$$\frac{1}{|\Gamma|} \int_{\Gamma} \frac{\partial u_{3D}}{\partial z} d\gamma = \frac{\partial u_{1D}}{\partial z} \Big|_{z=0}, \quad (13d)$$

$$-\frac{\partial^2 u_{1D}}{\partial z^2} + \gamma u_{1D} = 0 \quad z > 0, \quad (13e)$$

$$u_{1D}|_{z \rightarrow \infty} = 0, \quad (13f)$$

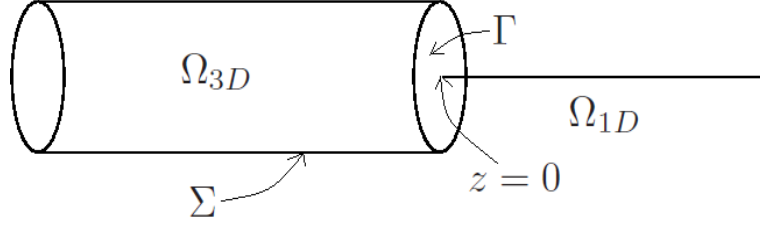


Figure 2: 3D-1D coupled subdomains.

where we have located the point  $z = 0$  at the 3D-1D interface.

For the solution of the previous problem, we consider again a generalized Schwarz method obtained by linearly combining the interface conditions (13c)-(13d) (notice that in this case the linear operators  $\mathcal{S}_{3D}$  and  $\mathcal{S}_{1D}$  are just multiplicative constants, and therefore coincide with their symbols  $\sigma_{3D}$  and  $\sigma_{1D}$  respectively):

Given  $\tilde{u}_{1D}^{(0)}$ , at each iteration  $n > 0$ , until convergence

1. solve the 3D problem in  $\Omega_{3D}$ :

$$-\Delta u_{3D}^{(n)} + \gamma u_{3D}^{(n)} = 0 \quad \mathbf{x} \in \Omega_{3D}, \quad (14a)$$

$$u_{3D}^{(n)}|_{\Sigma} = u_{3D}^{(n)}|_{z \rightarrow -\infty} = 0, \quad (14b)$$

$$\mathcal{S}_{3D} \frac{1}{|\Gamma|} \int_{\Gamma} u_{3D}^{(n)} d\gamma + \frac{1}{|\Gamma|} \int_{\Gamma} \frac{\partial u_{3D}^{(n)}}{\partial z} d\gamma = \mathcal{S}_{3D} \left( \tilde{u}_{1D}^{(n-1)} \Big|_{z=0} \right) + \frac{\partial \tilde{u}_{1D}^{(n-1)}}{\partial z} \Big|_{z=0}; \quad (14c)$$

2. solve the problem in  $\Omega_{1D}$ :

$$-\frac{\partial^2 u_{1D}^{(n)}}{\partial z^2} + \gamma u_{1D}^{(n)} = 0 \quad z > 0, \quad (15a)$$

$$u_{1D}^{(n)}|_{z \rightarrow \infty} = 0, \quad (15b)$$

$$\mathcal{S}_{1D} \left( u_{1D}^{(n)} \Big|_{z=0} \right) + \frac{\partial u_{1D}^{(n)}}{\partial z} \Big|_{z=0} = \mathcal{S}_{1D} \frac{1}{|\Gamma|} \int_{\Gamma} u_{3D}^{(n)} d\gamma + \frac{1}{|\Gamma|} \int_{\Gamma} \frac{\partial u_{3D}^{(n)}}{\partial z} d\gamma; \quad (15c)$$

3. relaxation step:  $\tilde{u}_{1D}^{(n)} = \omega u_{1D}^{(n)} + (1 - \omega) \tilde{u}_{1D}^{(n-1)}$ .

**Remark 1** We observe that the solution of the 3D problem (14) is not uniquely defined, since condition (14c) is defective, providing only one global information rather than one for each  $\mathbf{x} \in \Gamma$ . The numerical solution of defective problems has been intensively addressed e.g. in [24, 8, 39, 40, 42, 11, 12, 13, 44, 41, 34, 6, 28, 14, 15, 36], where suitable strategies to complete these conditions have been studied. In the numerical solution reported below, we made the following concrete choice to prescribe condition (14c):

$$\mathcal{S}_{3D}u_{3D}^{(n)} + \frac{\partial u_{3D}^{(n)}}{\partial z} = \mathcal{S}_{3D} \left( \tilde{u}_{1D}^{(n-1)} \Big|_{z=0} \right) + \frac{\partial \tilde{u}_{1D}^{(n-1)}}{\partial z} \Big|_{z=0}, \quad \mathbf{x} \in \Gamma. \quad (16)$$

### 3.1 Convergence analysis

We report in what follows a convergence analysis of the 3D-1D coupled problem (14)-(15). Again, we assume for the 3D solution independence of the angular variable. We have the following result.

**Proposition 4** The reduction factor related to iterations (14)-(15), in the case  $\omega = 1$  and  $u_{3D} = u_{3D}(r, z)$ , is given by

$$\rho_{3D-1D} = \sum_{k=1}^{\infty} \frac{4 (\sigma_{1D} + \beta_k) (\sigma_{3D} - \sqrt{\gamma})}{x_k^2 (\sigma_{1D} - \sqrt{\gamma}) (\sigma_{3D} + \beta_k)},$$

with

$$\beta_k = \sqrt{\gamma + \frac{x_k^2}{R^2}}. \quad (17)$$

**Proof.** Referring to Section 2.2, we have that the solution of the 3D problem (13a)-(13b) is given by

$$u_{3D}(r, z) = \sum_{k=1}^{+\infty} \widehat{u_{3D}}(k, z) J_0 \left( x_k \frac{r}{R} \right),$$

where the Fourier-Bessel coefficient is given by

$$\widehat{u_{3D}}(k, z) = C_{3D}(k) e^{\beta_k z},$$

with  $\beta_k$  given by (17). Instead, the 1D problem (13e)-(13f) is quickly solved by

$$u_{1D}(z) = C_{1D} e^{-\sqrt{\gamma} z}.$$

The application of the Fourier-Bessel expansion to the left-hand side of (16) and to the right-hand side (15c) leads to

$$\mathcal{S}_{3D}u_{3D}^{(n)}(r, 0) + \frac{\partial u_{3D}^{(n)}}{\partial z}(r, 0) = \sum_{k=1}^{\infty} (\sigma_{3D} + \beta_k) C_{3D}^{(n)}(k) J_0 \left( x_k \frac{r}{R} \right) \quad (18)$$

and to

$$\begin{aligned}
& \frac{\mathcal{S}_{1D}}{|\Gamma|} \int_{\Gamma} u_{3D}^{(n)} d\gamma + \frac{1}{|\Gamma|} \int_{\Gamma} \frac{\partial u_{3D}^{(n)}}{\partial z} d\gamma \\
&= \frac{2}{R^2} \sum_{k=1}^{+\infty} \left( \sigma_{1D} \int_0^R C_{3D}^{(n)}(k) J_0\left(x_k \frac{r}{R}\right) r dr + \int_0^R C_{3D}^{(n)}(k) \left( \frac{\partial}{\partial z} e^{\beta_k z} \right) \Big|_{z=0} J_0\left(x_k \frac{r}{R}\right) r dr \right) \\
&= \frac{2}{R^2} \sum_{k=1}^{+\infty} \left( (\sigma_{1D} + \beta_k) C_{3D}^{(n)}(k) \int_0^R J_0\left(x_k \frac{r}{R}\right) r dr \right) \\
&= \sum_{k=1}^{+\infty} (\sigma_{1D} + \beta_k) C_{3D}^{(n)}(k) \frac{2J_1(x_k)}{x_k}, \tag{19}
\end{aligned}$$

where the last identity follows from the formula  $\frac{d}{dx}(xJ_0(x)) = xJ_1(x)$ , see [27, page 103]. For  $X = 1, 3$  and for  $u_{XD}^n$  we obtain

$$\mathcal{S}_{XD} \left( u_{1D}^{(n)} \Big|_{z=0} \right) + \frac{\partial u_{1D}^{(n)}}{\partial z} \Big|_{z=0} = (\sigma_{XD} - \sqrt{\gamma}) C_{XD}^{(n)}.$$

Owing to the previous identity and to (18) and (19), the Robin interface conditions (16) and (15c) become

$$\sum_{k=1}^{\infty} (\sigma_{3D} + \beta_k) C_{3D}^{(n)}(k) J_0\left(x_k \frac{r}{R}\right) = (\sigma_{3D} - \sqrt{\gamma}) C_{1D}^{(n-1)} = (\sigma_{3D} - \sqrt{\gamma}) C_{1D}^{(n-1)} \sum_{k=1}^{\infty} \frac{2}{J_1(x_k) x_k} J_0\left(x_k \frac{r}{R}\right)$$

which becomes

$$(\sigma_{3D} + \beta_k) C_{3D}^{(n)}(k) = (\sigma_{3D} - \sqrt{\gamma}) C_{1D}^{(n-1)} \frac{2}{J_1(x_k) x_k},$$

and

$$\sum_{k=1}^{\infty} (\sigma_{1D} + \beta_k) C_{3D}^{(n)}(k) \frac{2J_1(x_k)}{x_k} = (\sigma_{1D} - \sqrt{\gamma}) C_{1D}^{(n)}.$$

This gives

$$\frac{C_{1D}^{(n)}}{C_{1D}^{(n-1)}} = \sum_{k=1}^{\infty} \frac{4}{x_k^2} \frac{(\sigma_{1D} + \beta_k)(\sigma_{3D} - \sqrt{\gamma})}{(\sigma_{1D} - \sqrt{\gamma})(\sigma_{3D} + \beta_k)}$$

and the thesis follows.  $\square$

### 3.2 Optimization procedures

First of all, we notice that the choice  $\sigma_{3D} = \sigma_{3D}^{opt} = \sqrt{\gamma}$  gives  $\rho_{3D-1D} = 0$ , and therefore convergence in two steps.

In order to fix an effective value for  $\sigma_{1D}$  for all the relevant  $k$ , we propose the following argument. Assume that, perhaps due to a measurement error, the

optimal choice of  $\sigma_{3D}$  differs from the exact value of  $\sqrt{\gamma}$  by a small quantity  $\varepsilon$ . Thus assume

$$\sigma_{3D} = \sqrt{\gamma} + \varepsilon.$$

This gives

$$\rho_{3D-1D} = \sum_{k=1}^{\infty} \frac{4}{x_k^2} \frac{\sigma_{1D} + \beta_k}{(\sigma_{1D} - \sqrt{\gamma})(\sqrt{\gamma} + \varepsilon + \beta_k)} \varepsilon.$$

When  $\varepsilon \rightarrow 0$ , each term

$$\frac{\sigma_{1D} + \beta_k}{(\sigma_{1D} - \sqrt{\gamma})(\sqrt{\gamma} + \varepsilon + \beta_k)} \varepsilon$$

is asymptotic to

$$\frac{\sigma_{1D} + \beta_k}{(\sigma_{1D} - \sqrt{\gamma})(\sqrt{\gamma} + \beta_k)} \varepsilon.$$

Our goal is now to search for the value of  $\sigma_{1D}$  that minimizes the maximum value

$$\max_{\beta_k \in [\beta_{k_{min}}, \beta_{k_{max}}]} \left| \frac{\sigma_{1D} + \beta_k}{(\sigma_{1D} - \sqrt{\gamma})(\sqrt{\gamma} + \beta_k)} \right|.$$

Observe that

$$\begin{aligned} & \max_{\beta_k \in [\beta_{k_{min}}, \beta_{k_{max}}]} \left| \frac{\sigma_{1D} + \beta_k}{(\sigma_{1D} - \sqrt{\gamma})(\sqrt{\gamma} + \beta_k)} \right| = \max_{\beta_k \in [\beta_{k_{min}}, \beta_{k_{max}}]} \left| \frac{1}{\sqrt{\gamma} + \beta_k} - \frac{1}{\sqrt{\gamma} - \sigma_{1D}} \right| \\ &= \max_{y \in \left[ \frac{1}{\beta_{k_{max}} + \sqrt{\gamma}}, \frac{1}{\beta_{k_{min}} + \sqrt{\gamma}} \right]} \left| y - \frac{1}{\sqrt{\gamma} - \sigma_{1D}} \right| \\ &= \begin{cases} \frac{1}{\beta_{k_{min}} + \sqrt{\gamma}} - \frac{1}{\sqrt{\gamma} - \sigma_{1D}} & \text{if } \frac{1}{\sqrt{\gamma} - \sigma_{1D}} \leq \frac{1}{2} \left( \frac{1}{\beta_{k_{max}} + \sqrt{\gamma}} + \frac{1}{\beta_{k_{min}} + \sqrt{\gamma}} \right) \\ -\frac{1}{\beta_{k_{max}} + \sqrt{\gamma}} + \frac{1}{\sqrt{\gamma} - \sigma_{1D}} & \text{if } \frac{1}{\sqrt{\gamma} - \sigma_{1D}} \geq \frac{1}{2} \left( \frac{1}{\beta_{k_{max}} + \sqrt{\gamma}} + \frac{1}{\beta_{k_{min}} + \sqrt{\gamma}} \right). \end{cases} \end{aligned}$$

Clearly, the value of  $\sigma_{1D}$  that minimizes the above quantity is the one for which

$$\frac{1}{\sqrt{\gamma} - \sigma_{1D}} = \frac{1}{2} \left( \frac{1}{\beta_{k_{max}} + \sqrt{\gamma}} + \frac{1}{\beta_{k_{min}} + \sqrt{\gamma}} \right) = \frac{\beta_{k_{min}} + \beta_{k_{max}} + 2\sqrt{\gamma}}{2(\beta_{k_{max}} + \sqrt{\gamma})(\beta_{k_{min}} + \sqrt{\gamma})},$$

that is

$$\sigma_{1D}^{opt} = \sqrt{\gamma} - \frac{2(\beta_{k_{max}} + \sqrt{\gamma})(\beta_{k_{min}} + \sqrt{\gamma})}{\beta_{k_{min}} + \beta_{k_{max}} + 2\sqrt{\gamma}}. \quad (20)$$

This gives the asymptotic (when  $\beta_{k_{min}} \neq \beta_{k_{max}}$ ), as  $\varepsilon \rightarrow 0$ ,

$$\rho_{3D-1D} \sim \left( \frac{1}{\beta_{k_{min}} + \sqrt{\gamma}} - \frac{1}{\beta_{k_{max}} + \sqrt{\gamma}} \right) \left( \sum_{k=k_{min}}^{k_{max}} \frac{2}{x_k^2} \right) \varepsilon =$$

$$\frac{\beta_{k_{max}} - \beta_{k_{min}}}{(\beta_{k_{min}} + \sqrt{\gamma})(\beta_{k_{max}} + \sqrt{\gamma})} \left( \sum_{k=k_{min}}^{k_{max}} \frac{2}{x_k^2} \right) \varepsilon.$$

Notice that if only one frequency is involved (i.e.  $\beta_{k_{min}} = \beta_{k_{max}} = \beta$ ), the optimal value (20) reduces to  $\sigma_{1D}^{opt} = -\beta$  and from the previous estimate of the reduction factor, we have  $\rho_{3D-1D} = 0$ .

### 3.3 Numerical results

The numerical results for the 3D part have been obtained by means of FreeFem++, whereas the 1D ones with *Matlab*.

We have considered  $\Omega_{3D} = \{(r, \varphi, z) : 0 \leq r < R, 0 \leq \varphi < 2\pi, -L < z < 0\}$ , with  $R = 1.0$  and  $L = 2.5$ , and  $\Omega_{1D} = (0, L)$ . The numerical solution in the 3D geometry has been obtained by solving a two-dimensional axi-symmetric problem in a rectangle. The corresponding meshes were formed by triangles. The stopping criterion corresponds to the residual of a block Gauss-Seidel scheme and it is given by (see [1]):

$$\left( \frac{1}{|\Gamma|} \int_{\Gamma} \left( \sigma_{3D} u_{3D}^{(n)} + \frac{\partial u_{3D}^{(n)}}{\partial z} \right) d\gamma - \sigma_{3D} u_{1D}^{(n)} - \frac{\partial u_{1D}^{(n)}}{\partial z} \right)^2 \leq \varepsilon^2,$$

where  $\varepsilon = 10^{-5}$ . We used P1 Finite Elements and we chose as initial guess  $\tilde{u}_{1D}^{(0)} = 1$ .

The value of the space discretization parameter was  $h = 0.05$ , so that the number of samples along the interface  $\Gamma$  was  $N = 20$  and, according to Sect. 2.4, we set  $k_{min} = 1$  and  $k_{max} = 10$  (i.e. we account for the dumping of the projection). We considered two values of the reaction parameter, namely  $\gamma = 1$  and  $\gamma = 10$ .

Referring to the quantities defined in Sect. 3.2, in Table 6 we report the results of the numerical experiments. In particular, for each scenario, we have considered four schemes: the Dirichlet-Neumann (DN,  $\sigma_{3D} = +\infty, \sigma_{1D} = 0$ ), the Neumann-Dirichlet (ND,  $\sigma_{3D} = 0, \sigma_{1D} = +\infty$ ), the Robin-Neumann (RN,  $\sigma_{3D} = \sigma_{3D}^{opt}, \sigma_{1D} = 0$ ), and the Robin-Robin (RR,  $\sigma_{3D} = \sigma_{3D}^{opt}, \sigma_{1D} = \sigma_{1D}^{opt}$ ) schemes.

$\gamma$	$\sigma_{3D}^{opt}$	$\sigma_{1D}^{opt}$	# iter DN	# iter ND	# iter RN	# iter RR
1	1.00	-5.47	X	11	3	2
10	3.16	-8.63	X	19	4	3

Table 6: Values of  $\sigma_{3D}^{opt}$  and  $\sigma_{1D}^{opt}$  and number of iterations for the four schemes considered. X means no convergence achieved.

We observe an excellent behavior of the Robin-based schemes in comparison with the classical ones. Moreover, the estimate provided by (20) seems to

improve the convergence properties of the optimized Robin-Robin scheme with respect to the Robin-Neumann one.

## Acknowledgements

CV has been partially supported by INDAM-GNCS and by the Italian MIUR PRIN12 project no. 201289A4LX “Modelli matematici e numerici del sistema cardiocircolatorio e loro applicazione in ambito clinico”.

## References

- [1] S. Badia, F. Nobile, and C. Vergara. Fluid-structure partitioned procedures based on Robin transmission conditions. *Journal of Computational Physics*, 227:7027–7051, 2008.
- [2] P. Blanco, M. Discacciati, and A. Quarteroni. Modeling dimensionally-heterogeneous problems: analysis, approximation and applications. *Numer. Math.*, 119:299–335, 2011.
- [3] P.J. Blanco, S. Deparis, and A.C.I. Malossi. On the continuity of mean total normal stress in geometrical multiscale cardiovascular problems. *J Comp Phys*, 51:136–155, 2013.
- [4] P.J. Blanco, R.A. Feijóo, and S.A. Urquiza. A unified variational approach for coupling 3d-1d models and its blood flow applications. *Computer Methods in Applied Mechanics and Engineering*, 196:4391–4410, 2007.
- [5] V. Dolean, M.J. Gander, and L. Gerardo Giorda. Optimized Schwarz Methods for Maxwell’s equations. *SIAM Journal of Scientific Computing*, 31(3):2193–2213, 2009.
- [6] V.J. Ervin and H. Lee. Numerical approximation of a quasi-newtonian Stokes flow problem with defective boundary conditions. *SIAM Journal on Numerical Analysis*, 45(5):2120–2140, 2007.
- [7] L. Formaggia, J.-F. Gerbeau, F. Nobile, and A. Quarteroni. On the coupling of 3D and 1D Navier-Stokes equations for flow problems in compliant vessels. *Computer Methods in Applied Mechanics and Engineering*, 191(6-7):561–582, 2001.
- [8] L. Formaggia, J.-F. Gerbeau, F. Nobile, and A. Quarteroni. Numerical treatment of defective boundary conditions for the Navier-Stokes equation. *SIAM Journal on Numerical Analysis*, 40(1):376–401, 2002.
- [9] L. Formaggia, A. Moura, and F. Nobile. On the stability of the coupling of 3d and 1d fluid-structure interaction models for blood flow simulations. *M2AN Math. Model. Numer. Anal.*, 41(4):743–769, 2007.

- [10] L. Formaggia, A. Quarteroni, and C. Vergara. On the physical consistency between three-dimensional and one-dimensional models in haemodynamics. *Journal of Computational Physics*, 244:97–112, 2013.
- [11] L. Formaggia, A. Veneziani, and C. Vergara. A new approach to numerical solution of defective boundary value problems in incompressible fluid dynamics. *SIAM Journal on Numerical Analysis*, 46(6):2769–2794, 2008.
- [12] L. Formaggia, A. Veneziani, and C. Vergara. Flow rate boundary problems for an incompressible fluid in deformable domains: formulations and solution methods. *Computer Methods in Applied Mechanics and Engineering*, 199 (9-12):677–688, 2009.
- [13] L. Formaggia and C. Vergara. Prescription of general defective boundary conditions in fluid-dynamics. *Milan Journal of Mathematics*, 80(2):333–350, 2012.
- [14] K. Galvin and H. Lee. Analysis and approximation of the cross model for quasi-newtonian flows with defective boundary conditions. *Appl. Math. Comp.*, 222:244–254, 2013.
- [15] K. Galvin, H. Lee, and L.G. Rebholz. Approximation of viscoelastic flows with defective boundary conditions. *J. Non Newt. Fl. Mech.*, 169-170:104–113, 2012.
- [16] M.J. Gander. Optimized Schwarz Methods. *SIAM Journal on Numerical Analysis*, 44(2):699–731, 2006.
- [17] M.J. Gander, F. Magoulès, and F.Nataf. Optimized Schwarz methods without overlap for the Helmholtz equation. *SIAM Journal of Scientific Computing*, 24:38–60, 2002.
- [18] M.J. Gander and Y. Xu. Optimized Schwarz Methods for circular domain decompositions with overlap. *SIAM Journal on Numerical Analysis*, 52(4):19812004, 2014.
- [19] M.J. Gander and Y. Xu. Optimized Schwarz Methods with nonoverlapping circular domain decomposition. *Math. Comp.*, in press, 2016.
- [20] L. Gerardo Giorda, F. Nobile, and C. Vergara. Analysis and optimization of Robin-Robin partitioned procedures in fluid-structure interaction problems. *SIAM Journal on Numerical Analysis*, 48(6):2091–2116, 2010.
- [21] G. Gigante, M. Pozzoli, and C. Vergara. Optimized Schwarz Methods for the diffusion-reaction problem with cylindrical interfaces. *SIAM Journal on Numerical Analysis*, 51(6):3402–3420, 2013.

- [22] G. Gigante and C. Vergara. Analysis and optimization of the generalized Schwarz method for elliptic problems with application to fluid-structure interaction. *Numer. Math.*, 131(2):369–404, 2015.
- [23] G. Gigante and C. Vergara. Optimized Schwarz method for the fluid-structure interaction with cylindrical interfaces. In T. Dickopf, M.J. Gander, L. Halpern, R. Krause, and L.F. Pavarino, editors, *Proceedings of the XXII International Conference on Domain Decomposition Methods*, pages 521–529. Springer, 2016.
- [24] J.G. Heywood, R. Rannacher, and S. Turek. Artificial boundaries and flux and pressure conditions for the incompressible Navier-Stokes equations. *International Journal for Numerical Methods in Fluids*, 22:325–352, 1996.
- [25] C. Japhet. Optimized Krylov-Ventcell method. Application to convection-diffusion problems. In P.E. Bjorstad, M.S. Espedal, and D.E. Keyes, editors, *Proceedings of the Ninth International Conference on Domain Decomposition Methods*, pages 382–389, 1998.
- [26] C. Japhet, N. Nataf, and F. Rogier. The optimized order 2 method. Application to convection-diffusion problems. *Fut Gen COmput Syst*, 18:17–30, 2001.
- [27] N. Lebedev. *Special Functions and Their Applications*. Courier Dover Publications, 1972.
- [28] H. Lee. Optimal control for quasi-newtonian flows with defective boundary conditions. *Computer Methods in Applied Mechanics and Engineering*, 200:2498–2506, 2011.
- [29] J.S. Leiva, P.J. Blanco, and G.C. Buscaglia. Partitioned analysis for dimensionally-heterogeneous hydraulic networks. *Mult Model Simul*, 9:872–903, 2011.
- [30] P.L. Lions. On the Schwarz alternating method III. In T. Chan, R. Glowinski, J. Periaux, and O.B. Widlund, editors, *Proceedings of the Third International Symposium on Domain Decomposition Methods for PDE's*, pages 202–223. Siam, Philadelphia, 1990.
- [31] F. Magoulès, P. Ivanyi, and B.H.V. Topping. Non-overlapping Schwarz method with optimized transmission conditions for the Helmholtz equation. *Computer Methods in Applied Mechanics and Engineering*, 193:4797–4818, 2004.
- [32] A.C.I. Malossi, P.J. Blanco, P. Crosetto, S. Deparis, and A. Quarteroni. Implicit coupling of one-dimensional and three-dimensional blood flow models with compliant vessels. *Multiscale Model Simul*, 11(2):474–506, 2013.

- [33] G. Papadakis. Coupling 3d and 1d fluid–structure–interaction models for wave propagation in flexible vessels using a finite volume pressure–correction scheme. *Comm Numer Meth Eng*, 25(5):533–551, 2009.
- [34] A. Porpora, P. Zunino, C. Vergara, and M. Piccinelli. Numerical treatment of boundary conditions to replace lateral branches in haemodynamics. *Int. J. Numer. Meth. Biomed. Eng.*, 28(12):1165–1183, 2012.
- [35] A. Qaddouria, L. Laayounib, S. Loiselc, J Cotea, and M.J. Gander. Optimized Schwarz methods with an overset grid for the shallow-water equations: preliminary results. *Appl. Num. Math*, 58:459–471, 2008.
- [36] A. Quarteroni, A. Manzoni, and C. Vergara. The cardiovascular system: Mathematical modeling, numerical algorithms, clinical applications. MOX-Report n. 38-2016, Dipartimento di Matematica, Politecnico di Milano, Italy, 2016.
- [37] A. Quarteroni, A. Veneziani, and C. Vergara. Geometric multiscale modeling of the cardiovascular system, between theory and practice. *Computer Methods in Applied Mechanics and Engineering*, 302:193–252, 2016.
- [38] B. Stupfel. Improved transmission conditions for a one-dimensional domain decomposition method applied to the solution of the Helmholtz equation. *Journal of Computational Physics*, 229:851–874, 2010.
- [39] A. Veneziani and C. Vergara. Flow rate defective boundary conditions in haemodinamics simulations. *International Journal for Numerical Methods in Fluids*, 47:803–816, 2005.
- [40] A. Veneziani and C. Vergara. An approximate method for solving incompressible Navier-Stokes problems with flow rate conditions. *Computer Methods in Applied Mechanics and Engineering*, 196(9-12):1685–1700, 2007.
- [41] C. Vergara. Nitsche’s method for defective boundary value problems in incompressible fluid-dynamics. *J Sci Comp*, 46(1):100–123, 2011.
- [42] I.E. Vignon-Clementel, C.A. Figueroa, K. Jansen, and C. Taylor. Out-flow boundary conditions for three-dimensional finite element modeling of blood flow and pressure waves in arteries. *Computer Methods in Applied Mechanics and Engineering*, 195:3776–3996, 2006.
- [43] Y. Yu, H. Baek, and G.E. Karniadakis. Generalized fictitious methods for fluid-structure interactions: Analysis and simulations. *Journal of Computational Physics*, 245:317–346, 2013.
- [44] P. Zunino. Numerical approximation of incompressible flows with net flux defective boundary conditions by means of penalty technique. *Computer Methods in Applied Mechanics and Engineering*, 198(37-40):3026–3038, 2009.

## MOX Technical Reports, last issues

Dipartimento di Matematica  
Politecnico di Milano, Via Bonardi 9 - 20133 Milano (Italy)

- 09/2017** Antonietti, P.F.; Ferroni, A.; Mazziere, I.; Paolucci, R.; Quarteroni, A.; Smerzini, C.; Stupazzini, N.  
*Numerical modeling of seismic waves by Discontinuous Spectral Element methods*
- 10/2017** Pini, A.; Stamm, A.; Vantini, S.  
*Hotelling's  $T^2$  in separable Hilbert spaces*
- 11/2017** Ferro, N.; Micheletti, S.; Perotto, S.  
*Anisotropic Mesh Adaptation for Crack Propagation Induced by a Thermal Shock*
- 12/2017** Gasperoni, F.; Ieva, F.; Barbati, G.; Scagnetto, A.; Iorio, A.; Sinagra, G.; Di Lenarda, A.  
*Multi state modelling of heart failure care path: a population-based investigation from Italy*
- 08/2017** Ambrosi, D.; Belousov, L.V.; Ciarletta, P.  
*Mechanobiology and morphogenesis in living matter: a survey*
- 07/2017** Cabassi A.; Pigoli D.; Secchi P.; Carter P.A.  
*Permutation tests for the equality of covariance operators of functional data with applications to evolutionary biology*
- 06/2017** Ekin, T.; Ieva, F.; Ruggeri, F.; Soyer, R.  
*On the Use of the Concentration Function in Medical Fraud Assessment*
- 05/2017** Menafoglio, A.; Hron, K.; Filzmoser, P.  
*Logratio approach to distributional modeling*
- 04/2017** Dede', L; Garcke, H.; Lam K.F.  
*A Hele-Shaw-Cahn-Hilliard model for incompressible two-phase flows with different densities*
- 02/2017** Arena, M.; Calissano, A.; Vantini, S.  
*Monitoring Rare Categories in Sentiment and Opinion Analysis - Expo Milano 2015 on Twitter Platform.*